

# Design, Fabrication, and Measurement Study of a Planar Phased Array Antenna

Ke Liu<sup>ID</sup>, Xiaotao Guo<sup>ID</sup>, Tianxin Liu<sup>ID</sup>, and Weilong Wang<sup>ID</sup>

**Abstract**—Phased array antenna (PAA) application in mobile communication is increasingly extensive, bringing a wide range of metrology requirements. The rotating-element electric-field vector (REV) method with circle fitting and linear fitting based on the complex measurement is proposed to calibrate the PAA. The simulation verifies the feasibility of the calibration method and the uncertainty contribution of the amplitude and phase fluctuation of the phase shifter to the array calibration and beamforming parameters. An  $8 \times 6$  patch array with a unique digital phase shifter for each element is designed for metrology research. The designed phased array is calibrated and measured in the anechoic chamber, with different initial phases of each element being programmable adjusted. The results show that the adjusted initial phases are calibrated accurately, and the array could be used for beamforming.

**Index Terms**—Beamforming, calibration, metrology, phase shifter, phased array antenna (PAA).

## I. INTRODUCTION

LARGE-SCALE antenna array system (AAS) or MIMO system is a vital notion in wireless communications, which plays a crucial role in 5G applications [1], [2], [3]. It has been verified that large-scale antenna arrays on the base station side generate directional beams to improve communication quality. As a result, the radiation pattern can be strengthened in a desired direction and at minimum in an undesired direction to meet more demanding specifications, such as high directivity and gain. AAS is usually realized as a phased array antenna (PAA), which produces a beam steered by adjusting the phase relationship between the array elements [4], [5]. PAA is widely used in 5G, and the metrology demands of the array have gradually increased.

Electronic scanning of the main beam is accomplished by changing the phase of exciting currents in each element antenna of the array, which is the most interesting part of the array antennas [4]. As a result, the main beams can be made to have high gain and low sidelobes. Furthermore, in beam scanning, a single main beam of an array is steered, and the direction can be varied continuously or in small discrete steps.

The parameters of the synthesized beam are directly affected by the amplitude and phase of each array element channel.

Manuscript received 5 February 2023; revised 28 May 2023; accepted 26 June 2023. Date of publication 19 July 2023; date of current version 31 July 2023. This work was supported by the National Key Research and Development Program of China under Grant 2021YFF0600302. The Associate Editor coordinating the review process was Dr. Djamel Allal. (Corresponding author: Ke Liu.)

The authors are with the Division of Electronics and Information Technology, National Institute of Metrology, Beijing 100029, China (e-mail: liuke@nim.ac.cn).

Digital Object Identifier 10.1109/TIM.2023.3296129

If the initial amplitude and phase consistency of each channel of the array antenna is poor, the parameters of the synthesized beam may not meet the design requirements. Therefore, many calibration methods are developed to measure the initial amplitude and phase of the array antenna, among which rotating-element electric-field vector (REV) methods are typical representatives [6], [7], [8], [9]. After calibration, each channel's initial amplitude and phase information can be obtained. In the subsequent beamforming or beam scanning, the initial differences in amplitude and phase parameters in all the elements channels are corrected according to the calibration results. Usually, a power amplifier achieves amplitude compensation, and a phase shifter performs phase compensation.

In addition to the consistency problem of the initial amplitude and phase of the array antenna, the phase shifter device also has amplitude and phase fluctuations with the phase being adjusted. And the amplifier device also has amplitude and phase fluctuations, with the amplitude changed.

Although there are many studies on the calibration of array antennas, the impact analysis of the uncertainty of synthesized beam parameters is rarely reported. The phase shifter is the core component of PAA. The effect of the amplitude and phase fluctuations caused by the adjustment of phase shifters on the synthesized beam is studied by simulation. Furthermore, to better study the metrology of PAA, we have developed a medium-scale array antenna platform, a set of 2-D planar patch antennae phased by digital phase shifter chips with the size of  $8 \times 6$  and carried out preliminary calibration and beamforming research of array antennas. This article is the extended version of the conference article in CPEM 2022 [10].

## II. PAA AND CALIBRATION

### A. Phased Array Antenna

The typical architecture of PAA usually consists of three parts, including a power distribution network, phase shifters, and radiation elements [11], [12], as shown in Fig. 1. The block diagram illustrates a 1-D array with  $N$  identical antenna elements, which are equally spaced by a distance  $d$  along an axis.

The diagram shows a typical phase array antenna. This example uses eight elements, each with a  $360^\circ$  phase shifter. A power distribution circuit provides an identical signal to each component. The direction of the combined signal can then be steered by varying the phase in each element according to a preset mathematical algorithm.

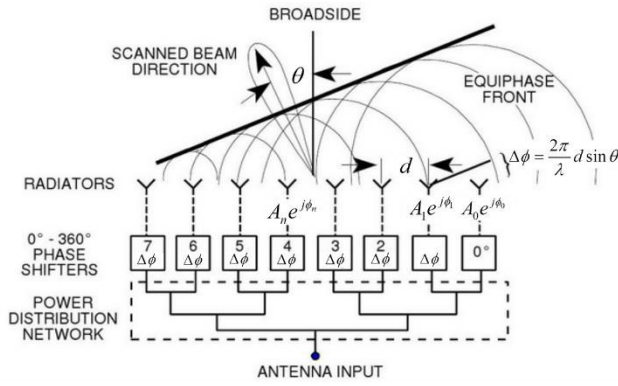


Fig. 1. Typical PAA architecture [11].

The array factor can be expressed as the following equation [4]:

$$S(\theta) = \sum_{n=0}^{N-1} A_n e^{j\phi_n} \cdot e^{jnk d \sin \theta} \quad (1)$$

where  $A_n$  and  $\phi_n$  denote the amplitude and phase of the  $n$ th exciting current, as shown in Fig. 1. Ideally, the feed signals to all the elements have identical amplitude and linear phase difference, that is,

$$A_n = A_0 \quad (2)$$

$$\phi_n = \phi_0 + n \cdot \Delta\phi. \quad (3)$$

The mainlobe direction (MLD)  $\theta$  and the linear phase difference  $\Delta\phi$  set by phase shifters satisfy the following relationship:

$$\Delta\phi = \frac{2\pi}{\lambda} d \sin \theta. \quad (4)$$

The power distribution network and phase shifter are not ideal, which will cause unequal signals from the antenna input port to all ports feeding to elements. Therefore, the signals fed to each antenna element will have amplitude and phase fluctuations

$$A_n = A_0 + \Delta A_{A,n} \quad (5)$$

$$\phi_n = \phi_0 + n \cdot \Delta\phi + \Delta\phi_{\phi,n}. \quad (6)$$

A 2-D array can be viewed as a composite of two 1-D arrays arranged linearly along two vertical axes. For a 2-D planar array with uniform spacing between adjacent elements, the array factor is given by

$$S(\theta, \varphi) = \sum_{m=-M_x}^{M_x} \sum_{n=-M_y}^{M_y} A_{mn} e^{j\phi_{mn}} e^{jk \sin \theta (m d_x \cos \varphi + n d_y \sin \varphi)} \quad (7)$$

where  $(\theta, \varphi)$  are the MLD of the 2-D array.

### B. Array Calibration

The inconsistency of the excitation signals in different paths makes the accurate element excitations unrealistic without phased array calibration. Various measurement techniques have been proposed for phased array calibration [13]. The objective of array calibration is to obtain the initial

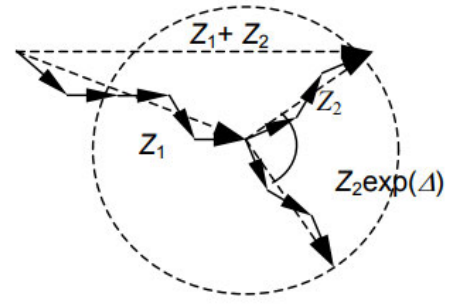


Fig. 2. Rotating and nonrotating composite field vectors.

amplitude and phase of the individual antenna elements and to compensate for the element-to-element variations for beam-forming. The well-known calibration methods for PAA are REV methods.

The REV method determines the amplitude and phase value of the electric field vector radiated from each element. When the phased array works as a transmit antenna, the composite field vector at a given observation point is a superposition of the field vectors of all the elements [14]. For example, suppose there is a 2-D uniform linear array, and the elements are divided into two groups. For one group, the phases of the elements are unchanged, while for the other group, the phases of the elements are changed by their phase shifters with the same steps. Then, the composite vector for the latter group would rotate and draw a circle, like a vector  $Z_2$  in Fig. 2. By rotating more than three positions, the ring can be determined or fit, and the rotating vector can be obtained.

According to the type of measurement signals, REV methods could be divided into complex and amplitude-only measurements. Although the latter method could avoid the problem of inaccurate phase measurement, it would introduce the problem of the binary solution of the equation. Usually, the ambiguity of solutions could be eliminated if the amplitude of REV is less than that of non-REV [6], [9]. But this relationship is sometimes difficult to meet, for example, for the composite REV method. The combined REV method synchronously alters the phases of a group of elements, could improve the signal-to-noise ratio [9], and is suitable for calibrating large-scale phased arrays. However, in this method, the amplitudes of the REV and non-REV are comparable, which may make it difficult to determine the appropriate value between the two values. After comparative analysis, we adopt the composite REV method based on complex measurements to calibrate PAA.

If grouped according to specific rules, multiple rotation vectors can be obtained, and the associated vector of each element can be obtained by solving the equation system. The Hadamard matrix is a binary orthogonal matrix used as a grouping scheme [9]. Fig. 3 shows a case of the Hadamard matrix for the grouping scheme of a 48-element array. In this figure, the blue pixel representing “0” means nonrotation of the corresponding element vector, and the yellow pixel representing “1” means rotation of the related element vector. Each row corresponds to a rotating scheme and corresponds to a composite REV. Half of the elements participate in the rotation

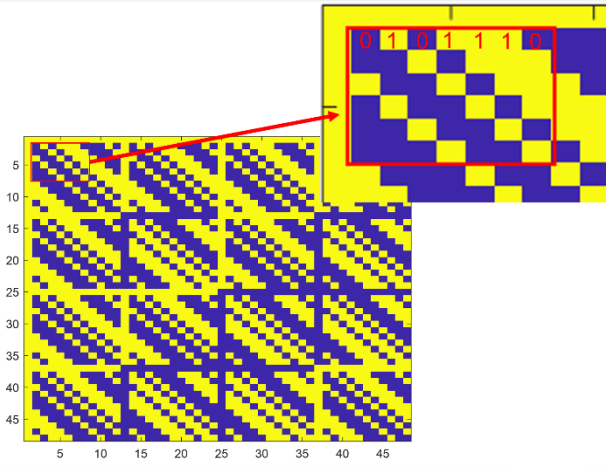


Fig. 3. Case of Hadamard matrix with a size of  $48 \times 48$ .

for each rotation scheme after the first row of the matrix. At least three phases are altered for the group of elements labeled “1,” and vector network analyzer (VNA) acquires the composite REV as the amplitude and phase format. The composite REV is then determined by two fitting methods: amplitude achieved by circle fitting and phase completed by linear fitting.

### III. SIMULATION

A planar PAA with  $n \times m$  size is simulated to verify the composite REV method based on the complex measurement and then be used for uncertainty analysis of the array factor's beam parameters.

#### A. Generate Measurement Data

The path from the input to each radiator in Fig. 1 is denoted as the element channel. The following two sets of data are simulated.

- 1) The initial amplitude and phase for each element channel.
- 2) The measured complex  $S_{21}$  data for composite REV.

The steps for simulation data generation are as follows.

- 1) Set the scale of PAA as  $(n, m)$  ( $n$  and  $m$  denote column and row for the array, respectively).
- 2) Produce  $mn$  random normalized amplitudes with a uniform distribution between  $(0.9-1.1)$  and  $mn$  random phases with a uniform distribution between  $(0^\circ-360^\circ)$ . The  $mn$  amplitudes and phases are the initial element channels' complex parameters.
- 3) Produce  $mn$  Hadamard matrix.
- 4) Set the working frequency, measurement displacement between the array and probe, the altering phases for the composite REV test, and the maximum allowable errors of amplitude and phase (EAP) for phase shifting.
- 5) Produce complex  $S_{21}$  data between the input of the array and the probe according to Hadamard matrix schemes and the altering phases.  $S_{21}$  is the vector summation of all the elements, including the different amplitudes and phases induced by: a) the displacements between each element and the probe and b) the amplitude and phase errors with uniform distribution for phase shifting.

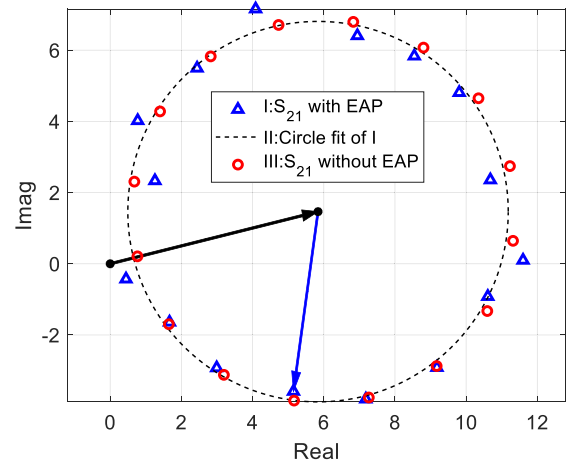


Fig. 4. Circle fitting according to one row of the Hadamard matrix.

The planar array with six rows and eight columns with a center frequency of 3.6 GHz is configured. The elements are equally spaced by  $0.6 \lambda$  along the  $x$ - and  $y$ -axes. The mutual coupling between elements is less than  $-15$  dB. The measurement data is complex  $S_{21}$  by VNA with a probe facing the array at a distance of 3.5 m. Two measurement data are generated without EAP of phase shifters and with EAP, respectively. For the measurement data with EAP, the amplitude error of the phase shifter is set to 1 dB, and the phase error is fixed to  $11.2^\circ$ .

#### B. Calculate and Analysis

The amplitude of composite REV is obtained by circle fitting and takes the radius of the fit circle shown in Fig. 4. The black arrow in the figure means the non-REV.

The symbols of the blue triangle denote the measured  $S_{21}$  with 16 synchronous phases altering the specified phase shifters. The amplitudes and phases of the phase shifters would fluctuate with changing the phases, and the measured composite vectors are distributed around the fitting circle. Taking the ideal measurement  $S_{21}$  (represented by symbols of the red circles, which assumed that phase shifters have no amplitude and phase setting errors) as references, the values of the fit ring are more stable and accurate than the measured  $S_{21}$ . So, taking the radius of the fit circle as the amplitude of the composite REV is an appropriate choice.

The measured  $S_{21}$  with EAP are not equally angle spaced around the fitting circle in Fig. 4. We would obtain a more stable and accurate initial phase by the linear fitting of the phases of the REV's.

The 16 phase parameters measured  $S_{21}$  relative to the center of the fit circle, as shown in Fig. 4, are used to fit a straight line, shown in Fig. 5. The phases are processed by unwrapping. The phases with and without EAP do not coincide with each other. We observe their differences by looking at their phase differences. Same as above, taking the ideal phases (represented by symbols of the red circles, legend III: Phases without EAP) as references, the phase differences for the fit line noted by the magenta dashed line (legend V: II and III) are less than that for measured  $S_{21}$  noted by the blue dashed

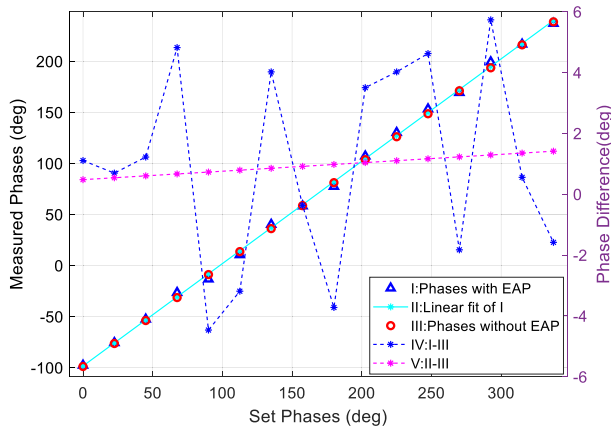


Fig. 5. Phase linear fitting according to one row of Hadamard matrix.

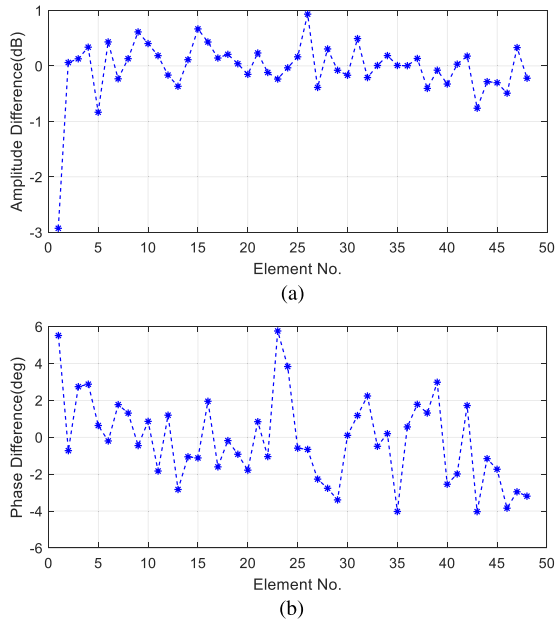


Fig. 6. Differences between the calibrated values and the set values for (a) amplitude and (b) phases of 48 elements.

line (legend IV: I–III). So, taking the fit line's initial phase as the composite REV's initial phase is appropriate.

Figs. 4 and 5 are examples of obtaining a composite REV by analyzing the measurement data according to the grouping scheme corresponding to one row of the Hadamard matrix. Doing the same for each matrix row would yield 48 composite REV's. These 48 composite REV's and the Hadamard matrix could establish linear equations, and the corresponding vectors of the 48 elements would be obtained by solving the system of equations. Fig. 6 shows the differences between the calibrated amplitudes and the set amplitudes of the 48 elements and the differences between the calibrated phases and the set phases.

It can be seen that the amplitude differences are mainly distributed within the range of  $\pm 1$  dB, and the phase differences are primarily distributed within  $\pm 5^\circ$ . They are comparable to the set errors of amplitude and phase of the phase shifters.

After obtaining the array element's initial amplitude and phase data by REV calibration, the subsequent beamforming can be performed with amplitude and phase compensation.

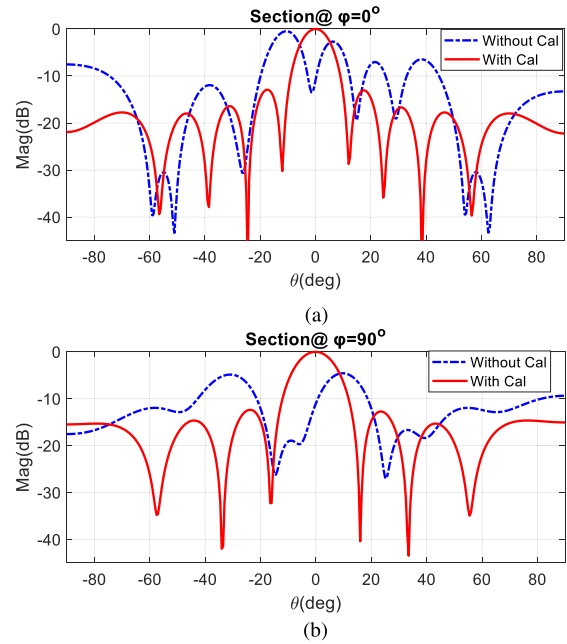


Fig. 7. Synthesized beam with the mainlobe pointing to the direction at  $\theta = 0^\circ$  for (a)  $\varphi = 0^\circ$  section and (b)  $\varphi = 90^\circ$  section.

Due to cost considerations, the PAA we developed later can only adjust the phase, not the amplitude. Here, when we do beamforming research, we only do phase compensation. The synthesized beam is formed with the main beam pointing to the direction at  $\theta = 0^\circ$  in Fig. 7. It can be found that the expected pattern does not form without calibration, but the beam features such as the main beam, sidelobes, and nulls are very clear with calibration.

Furthermore, we analyze the contribution of the uncertainty of the initial amplitude and phase calibration of the array and the uncertainty of the beamforming parameters due to the amplitude and phase fluctuations of the phase shifters. Assume that amplitude and phase fluctuations are evenly distributed in  $(-0.5$  to  $0.5)$  dB and  $(-5.6$  to  $5.6)^\circ$ , respectively. 10 000 Monte Carlo method (MCM) simulations are used to analyze the uncertainties of the calibrated amplitudes and phases and the uncertainties of the beamforming parameters.

The calibrated amplitudes and phases with standard uncertainties of all elements are shown in Fig. 8(a) and (b), respectively. The calibrated amplitudes in Fig. 8(a) are normalized to the setting amplitudes to compare the results between each array element. The calibrated phases in Fig. 8(b) are differences between calibrated and setting phases. The calibration results show that the calibration amplitudes and phases of elements are mainly distributed around 0, indicating that the calibration and set values have a good consistency. Except for the first element, the uncertainties of the amplitudes are less than 0.5 dB, and the uncertainties of the phases are mainly less than  $3^\circ$ . As can be seen in Fig. 3, the first column of the Hadamard matrix is all 1, while half of the remaining columns are 1 and the other half is 0. Thus, when solving the initial value of the amplitude phase, array element one is involved in the calculation of all equations, and the other array elements are only interested in the computation of half



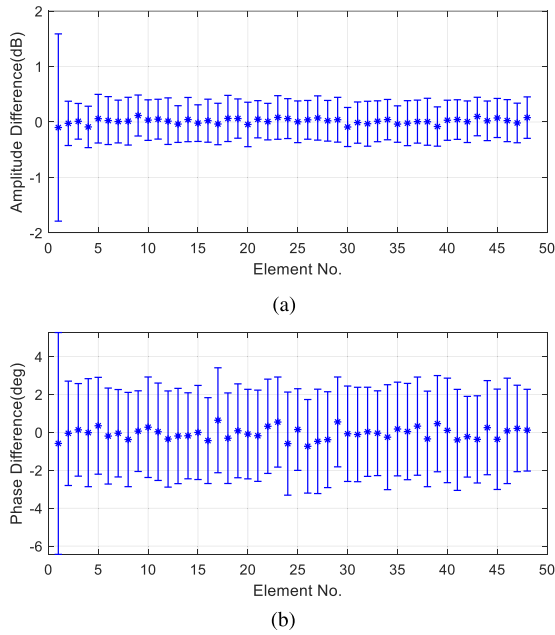


Fig. 8. Deviations with standard uncertainties of (a) calibrated amplitudes and (b) calibrated phases for all elements.

of the equations. In the whole process, the error accumulation of array element one is larger than that of other elements, and thus the amplitude and phase fluctuations of the solved array element are also larger.

For synthesized beams, three parameters are mainly considered: MLD, sidelobe level, and half-power beamwidth (HPBW). Histograms of these three parameters in the section  $\varphi = 0^\circ$  are shown in Fig. 9. The distribution of the MLDs and HPBWs are relatively concentrated, indicating that they are less affected by the amplitude and phase fluctuations of the phase shifters. The MLDs are in the range of  $(-0.1$  to  $0.1)^\circ$ , and HPBWs are mainly in the field of  $(10.685$ – $10.7)^\circ$ . The distribution of the sidelobe levels is relatively more comprehensive, but it is also distributed primarily in the range of about 0.6 dB between  $-13.1$  and  $-12.5$  dB.

The three parameters of the synthesized beams in sections  $\varphi = 0^\circ$  and  $\varphi = 90^\circ$  are listed in Table I. Due to the different numbers of array elements along the  $x$ - and  $y$ -directions of the array, the antenna apertures in the two directions are different, and the widths of the synthesized beam in the two sections are also different.

#### IV. FABRICATION OF PAA

An  $8 \times 6$  planar microstrip PAA with a central working frequency of 3.6 GHz is designed and fabricated. The structure of PAA is mainly composed of three parts, as shown in Fig. 1: radiating elements, phase shifters, and power distribution network.

##### A. Radiating Element

A typical microstrip antenna consists of a radiating patch, a substrate layer, and a backplane ground layer. The stacked parasitic patch is adopted to broaden the operating frequency bandwidth, as shown in Fig. 10. The element's key parameters are listed in Table II.

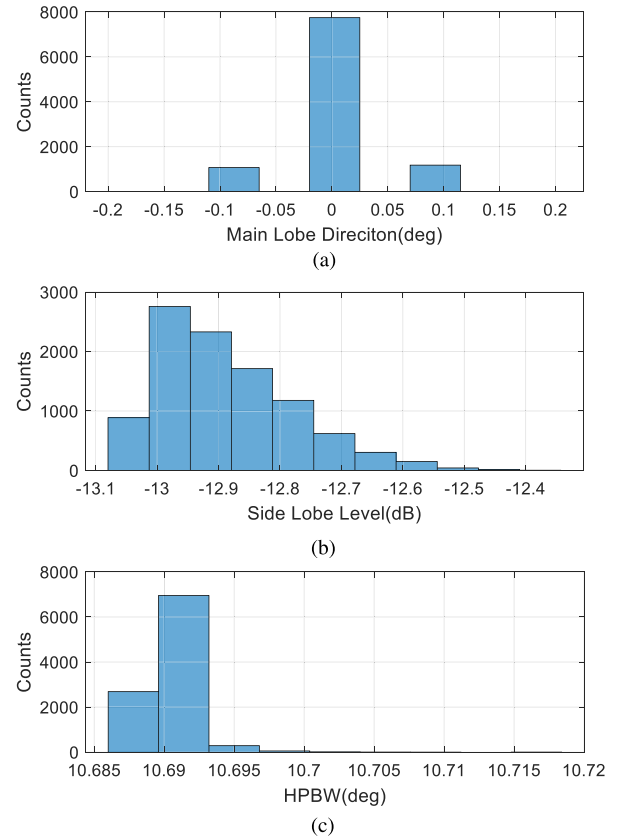


Fig. 9. Histograms of (a) MLD, (b) sidelobe level, and (c) HPBW of the synthesized beams in section  $\varphi = 0^\circ$ .

TABLE I  
BEAM PARAMETERS OF MCM SIMULATIONS

Section		Main lobe (deg)	HPBW (deg)	Side Lobe (dB)
$\varphi=0^\circ$	Exp.	0.001	10.691	-12.89
	$u$	0.048	0.002	0.11
$\varphi=90^\circ$	Exp.	0.007	14.287	-12.43
	$u$	0.069	0.002	0.09

Note: Exp. is short for expectation,  $u$  stands for standard uncertainty.

The radiating patches marked “(2)” and “(3)” in Fig. 10 are made of copper. The dielectric substrate of the upper parasitic unit of the microstrip antenna marked “(4)” is Rogers 4730, and the substrate of the lower unit marked “(1)” is designed with Rogers 4350B laminated board. The microstrip antenna is simulated in the range of  $(3.4$ – $3.8)$  GHz. The voltage standing wave ratio (VSWR) are less than 1.3, and gains are more significant than 8.0 dBi. The HPBWs are about  $80^\circ$  for horizontally polarized (HP) and  $68^\circ$  for vertically polarized (VP).

##### B. Phase Shifters

The designed PAA adopts an HMC648a chip from Analog Devices Inc. (ADI) as the phase shifter. This chip is a six-bit digital phase shifter that is rated from  $(2.9$ – $3.9)$  GHz, providing  $360^\circ$  of phase coverage, with a least significant bit (LSB) of  $5.625^\circ$ . In addition, the chip is made of GaAs

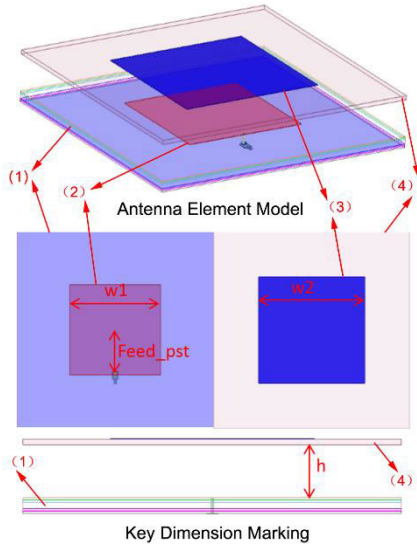


Fig. 10. Microstrip antenna element with a stacked parasitic patch.

TABLE II  
DIMENSIONS OF THE ANTENNA ELEMENT

Parameter	Value/mm
w1	23.2
w2	27
Feed_pst	11
h	7

and features a deficient rms phase error of  $1.2^\circ$  and a typical phase error of  $5^\circ$ .

### C. Power Distribution Network

The feed network is a radio-frequency link used to distribute the RF input power to each antenna element equally. Here, the Wilkinson divider is designed as the power distribution network. For the  $8 \times 6$  array, it is necessary to design a 1-to-48 power divider. Such a large-scale divider can be simplified by cascade design with several levels of 1-to-2 and 1-to-3 dividers.

### D. Phased Array Antenna

The available photographs of fabricated PAA are shown in Fig. 11.

Fig. 11(f) shows the assembled array antenna, and Fig. 11(a)–(e) shows the details of its different parts. The front panel marked “(1)” in Fig. 11(f) is a parasitic element array in Fig. 11(a) to increase the system bandwidth. Fig. 11(b) and (c) shows the front and rear of the core PAA board, corresponding to the second board marked “(2)” of Fig. 11(f). The second board’s substrate is laminated, and its inside copper layer is the backplane ground layer. A separate board called a phase control board with general-purpose input–output (GPIO) is designed to manage all the pins for level adjustment and power supply of phase shifter chips. Fig. 11(d) and (e) shows the front and rear of the phase control board, corresponding to the third board marked “(3)” of Fig. 11(f). Two plug interfaces

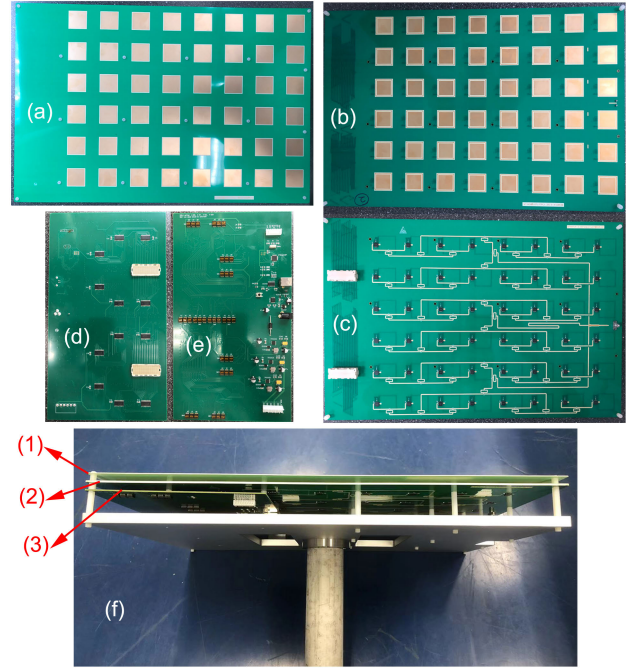


Fig. 11. Photographs of the fabricated PAA. (a) Front of the parasitic element array. (b) Front of core PAA board. (c) Rear of core PAA board. (d) Front of phase control board. (e) Rear of phase control board. (f) Assembled array antenna.

connect the phase control board to the core PAA board. A PC could control the PAA through Universal Serial Bus (USB) port connected to the phase control board.

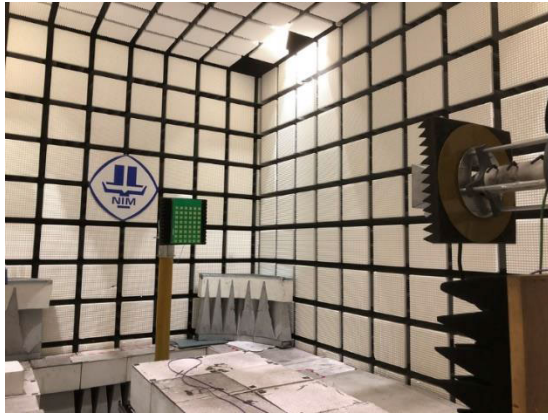
## V. MEASUREMENT

The beamforming and calibration experiments of the manufactured PAA are carried out in the anechoic chamber at the National Institute of Metrology (NIM), Beijing, China, shown in Fig. 12(a). The antenna array is mounted VP on the turntable, with its center aligned to the probe antenna (R&S<sup>1</sup>HF907). The PAA is connected to a PC out of the chamber via a long USB cable. The developed software shown in Fig. 12(b) runs on the PC to control the elements’ phases to achieve array calibration and beamforming.

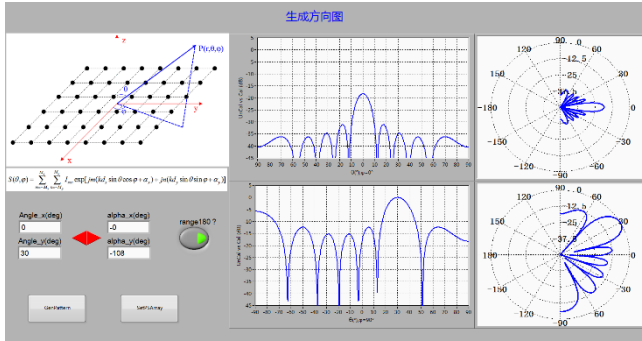
### A. Beamforming

The amplitudes of the fabricated array’s elements are not adjustable, and beamforming is realized by controlling the elements with equal phase differences. The beam steering range of the designed array covers  $(-30^\circ-30^\circ)$ , and the gain drop is no bigger than 2 dB with beam steering in this range. The patterns of multiple beam states are measured for HP and VP, respectively. The measurement results in Fig. 13 show that the mainlobe and sidelobes are clear for HP and VP, and the steering range meets the design requirements. The gain drop of  $\pm 30^\circ$  steering beam is up to 1.2 dB, as shown in Table III, which indicates that the mutual coupling effect between the elements is weak. It is worth mentioning that the formed beams are realized without initial phase calibration, which reflects that the phase consistency of each element channel of the array is relatively good.

<sup>1</sup>Registered trademark.



(a)



(b)

Fig. 12. (a) Measurement setup of PAA in an anechoic chamber and (b) software for calibration and beamforming.

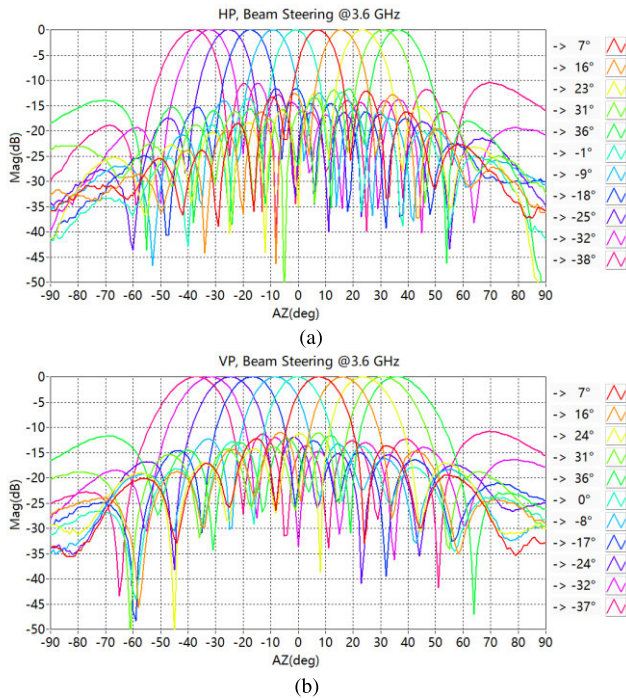


Fig. 13. Beam steering for (a) HP and (b) VP.

### B. Calibration

The beam parameters' variations induced by amplitude imbalance are less than phase imbalance [15], and only the initial phases of the fabricated array are calibrated by the

TABLE III  
GAINS FOR BEAM STEERING AT 3.6 GHz

HP	MLD (°)	Gain (dBi)	VP	MLD (°)	Gain (dBi)
	-32	13.9		-32	13.9
	-25	14.7		-24	14.6
	-18	14.6		-17	14.5
	-9	14.6		-8	14.6
	-1	15.1		0	15.2
	7	14.8		7	14.7
	16	14.7		16	14.5
	23	14.9		24	14.8
	31	14.3		31	14.1

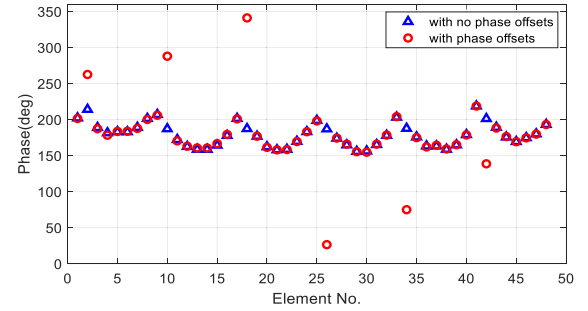


Fig. 14. Estimated initial phases by REV calibration.

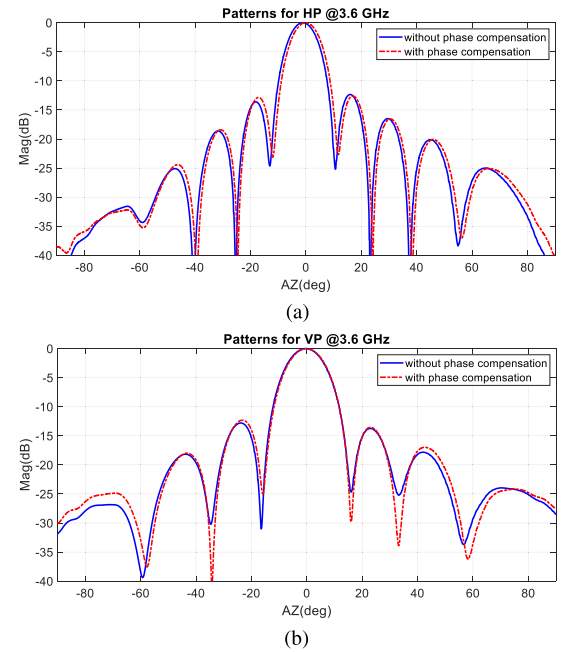


Fig. 15. Two-dimensional patterns without and with phase compensation for (a) HP and (b) VP.

proposed REV method mentioned above. Since the array antenna is designed to maintain the consistency of the transmission line length of each array element channel, the calibrated initial phases' distribution is concentrated, and the biggest phase difference is less than  $60^\circ$ , represented by the blue triangles in Fig. 14. The elements of the 2-D array are consecutively numbered by row first, corresponding to the placement in Fig. 11(a).



TABLE IV  
PHASE OFFSETS FOR SIX ELEMENTS (°) IN THE SECOND COLUMN

No.	1	2	3	4	5	6	7	8
1	0	50	0	0	0	0	0	0
2	0	100	0	0	0	0	0	0
3	0	150	0	0	0	0	0	0
4	0	200	0	0	0	0	0	0
5	0	250	0	0	0	0	0	0
6	0	300	0	0	0	0	0	0

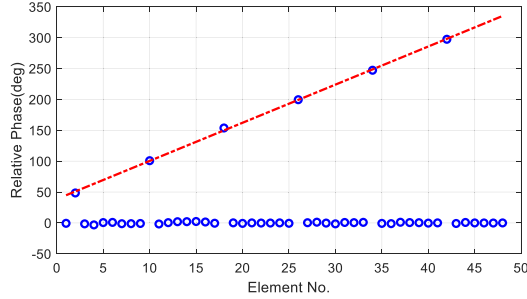


Fig. 16. Calibrated phases by the proposed REV method.

The patterns without and with phase compensation are close, as shown in Fig. 15, but the latter has a more accurate MLD for HP and better null depths for VP.

To verify the calibration algorithm more clearly, the initial phases can be changed by adding some appropriate phase offsets on specific array elements in Table IV by phase shifters. The symbols of the red circle in Fig. 14 denote the calibrated initial phases with phase offsets. The figure shows that except for the six elements with phase offsets, the phase position of the remaining elements almost coincides with the phase before the offset phases are set.

The calibrated phase offsets shown in Fig. 16 are relative phases, which are differences between phase calibration results with and without additional phase offsets.

The phase offsets for Nos. 2, 10, 18, 26, 34, and 42 are consistent with the set values in Table IV. The maximum difference is about  $3.7^\circ$  for element No. 18. The patterns without and with phase compensation are significantly different, especially for HP, shown in Fig. 17.

It should be noted that the PAA is measured at a distance of about 3.5 m from the probe, which is not performed under far-field conditions. The anechoic chamber space shown in Fig. 12(a) is about 8.2 (length)  $\times$  5.0 (width)  $\times$  5.0 m (height), and the distance between the antenna tower and the DUT turntable can be adjusted to about 4 m at most. The aperture size for this designed array antenna is about 0.5 m, the working center frequency is 3.6 GHz, and the required far-field distance is about 6 m according to the far-field calculation formula ( $R = 2D^2/\lambda$ ) [4]. However, the measured pattern shows that the synthetic beam has been formed compared to the ideal pattern shown in Fig. 18.

An ideal array pattern is the product of the array factor and the element pattern. The mainlobes' complete coincidence and the secondary lobes' proximity indicate that the mutual coupling effect between the elements is weak. Nulls are not deep enough, indicating that far-field conditions are insufficient.

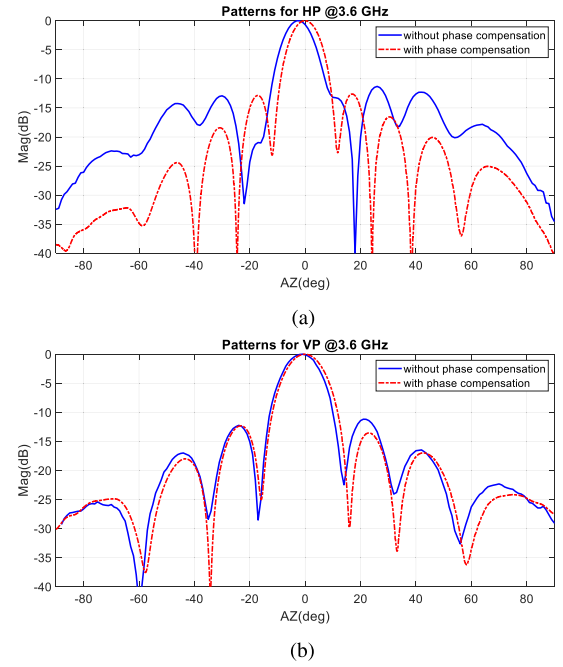


Fig. 17. Two-dimensional patterns without and with phase compensation for (a) HP and (b) VP of the array with phase offsets in Table IV.

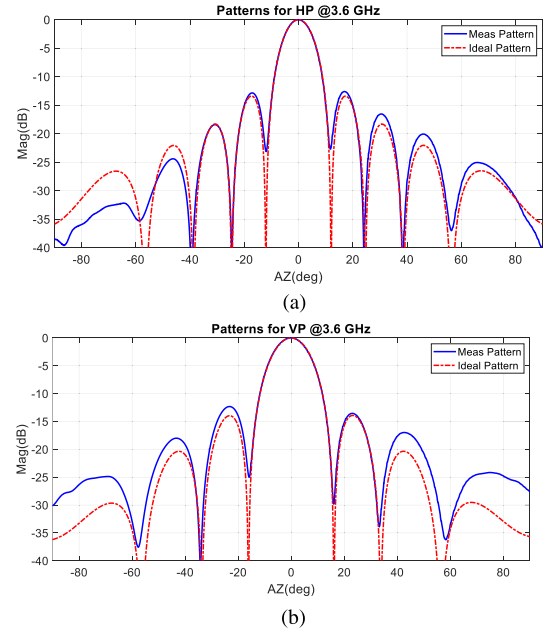


Fig. 18. Measured and ideal patterns for (a) HP and (b) VP.

However, it does not affect the preliminary experimental study of calibration and beamforming. For future research, we must thoroughly consider far-field or near-field conditions and improve calibration and beamforming measurement accuracy.

## VI. CONCLUSION

The composite REV method based on the complex measurement is proposed to calibrate the PAA. The composite REVs are determined by circle fitting and linear fitting, avoiding the problem of distinguishing between two values. Furthermore, MCM is adopted to analyze the contributions of the uncertainty of the initial amplitude and phase calibration of the



array and the uncertainty of the beamforming parameters due to the amplitude and phase fluctuations of the phase shifters.

A planar PAA is designed and fabricated. The designed array has independent 6-bit phase adjustment, suitable for researching various calibration and beamforming algorithms. In addition, it is platform would be further used for beamforming and other metrology research.

## REFERENCES

- [1] K. A. Remley et al., "Measurement challenges for 5G and beyond: An update from the National Institute of Standards and Technology," *IEEE Microw. Mag.*, vol. 18, no. 5, pp. 41–56, Jun. 2017.
- [2] Y. Wang, S. Zhang, H. Cen, and B. Zou, "Performance analysis and improvement of large-scale antenna array system," *J. Intell. Fuzzy Syst.*, vol. 38, no. 1, pp. 481–486, Jan. 2020.
- [3] A. K. Vallappil, M. K. A. Rahim, B. A. Khawaja, N. A. Murad, and M. G. Mustapha, "Butler matrix based beamforming networks for phased array antenna systems: A comprehensive review and future directions for 5G applications," *IEEE Access*, vol. 9, pp. 3970–3987, 2021.
- [4] W. L. Stutzman and G. A. Thiele, *Antenna Theory and Design*. Hoboken, NJ, USA: Wiley, 2012.
- [5] R. J. Mailloux, *Phased Array Antenna Handbook*. Norwood, MA, USA: Artech House, 2017.
- [6] R. Long, J. Ouyang, F. Yang, W. Han, and L. Zhou, "Fast amplitude-only measurement method for phased array calibration," *IEEE Trans. Antennas Propag.*, vol. 65, no. 4, pp. 1815–1822, Apr. 2017.
- [7] B. Wang, Y. Li, and B. Tian, "Rotating-element electric-field vector(REV) calibration method based on power measurement for phased array antenna," in *Proc. Int. Appl. Comput. Electromagn. Soc. Symp. (ACES)*, Aug. 2017, pp. 1–2.
- [8] H.-J. Yoon and B.-W. Min, "Improved rotating-element electric-field vector method for fast far-field phased array calibration," *IEEE Trans. Antennas Propag.*, vol. 69, no. 11, pp. 8021–8026, Nov. 2021.
- [9] M. Liu and Z. Feng, "Combined rotating-element electric-field vector (CREV) method for nearfield calibration of phased array antenna," in *Proc. Int. Conf. Microw. Millim. Wave Technol.*, Apr. 2007, pp. 1–4.
- [10] K. Liu, X. Guo, T. Liu, and W. Wang, "Design and calibration of a planar phased array," in *Proc. Conf. Precis. Electromagn. Meas.*, Wellington, New Zealand, 2022, pp. 1–2.
- [11] S. S. Hreshee, "Design and analysis of new optical beamforming matrix for phased array antenna," in *Proc. Int. Conf. Adv. Technol. Sci.*, Antalya, Turkey, 2014, pp. 1015–1018.
- [12] R. L. Haupt and M. Lanagan, "Reconfigurable antennas," *IEEE Antennas Propag. Mag.*, vol. 55, no. 1, pp. 49–61, Feb. 2013.
- [13] M. A. Salas-Natera, R. M. Rodriguez-Osorio, and L. de Haro, "Procedure for measurement, characterization, and calibration of active antenna arrays," *IEEE Trans. Instrum. Meas.*, vol. 62, no. 2, pp. 377–391, Feb. 2013.
- [14] R. Yonezawa, Y. Konishi, I. Chiba, and T. Katagi, "Beam-shape correction in deployable phased arrays," *IEEE Trans. Antennas Propag.*, vol. 47, no. 3, pp. 482–486, Mar. 1999.
- [15] K. Liu, X. Bian, S. Wang, and H. Zhao, "Measurement uncertainty of beam parameters induced by imbalances of amplitude and phase for antenna array," in *Proc. Conf. Precis. Electromagn. Meas. (CPEM)*, Aug. 2020, pp. 1–2.



**Ke Liu** was born in Henan, China, in 1981. He received the B.S. and Ph.D. degrees in biomedical engineering from Tsinghua University, Beijing, China, in 2004 and 2009, respectively.

He is an Associate Research Professor with the Division of Electronics and Information Technology, National Institute of Metrology, Beijing. His research interests include antenna and propagation metrology, over-the-air (OTA) tests, and reverberation chamber design and measurement.



**Xiaotao Guo** was born in Hubei, China, in 1986. He received the B.S. degree in telecommunications engineering and the Ph.D. degree in physical electronics from the Beijing University of Posts and Telecommunications, Beijing, China, in 2008 and 2013, respectively.

He is an Associate Research Professor with the Division of Electronics and Information Technology, National Institute of Metrology, Beijing. His current research interests include reverberation chamber design and measurement, over-the-air (OTA) tests, and antenna and propagation metrology.



**Tianxin Liu** was born in Gansu, China, in 1992. He received the B.S. degree in information and communication engineering from the China Academy of Telecommunications Technology, Beijing, China, in 2018.

He is a Research Assistant with the Division of Electronics and Information Technology, National Institute of Metrology, Beijing. His research interests include over-the-air (OTA) tests, antenna and propagation metrology, and reverberation chamber design and measurement.



**Weilong Wang** was born in Beijing, China, in 1964. He received the B.S. degree in wireless communication engineering from Beijing Jiaotong University, Beijing, in 2005.

He is a Research Professor with the Division of Electronics and Information Technology, National Institute of Metrology, Beijing. His current research interests include antenna and propagation metrology and electromagnetic compatibility (EMC).